Hybrid Analytical Model for Predicting the Electromagnetic Losses in Surface-Mounted Permanent-Magnet Motors

Zhaokai Li, *Member*, *IEEE*, Xiaoyan Huang*, *Member*, *IEEE*, Jun Ma, Zhuo Chen, Ang Liu, and
Luca Peretti, *Senior Member, IEEE*

Abstract—**This paper presents a comprehensive method to predict the electromagnetic losses in surface-mounted permanent-magnet motors based on a hybrid analytical model. Hybrid analytical model will significantly improve the calculation speed compared with finite-element method while keeping great accuracy, making it a competitive alternative for the analysis and optimization of permanent-magnet motors. As the accurate field distribution is the bias of electromagnetic losses prediction, the magnet loss, sleeve loss, and copper loss can all be accurately obtained from their vector potential distribution using hybrid analytical model with small computational burden. As for iron loss, the improved Jiles-Atherton model is proposed to build the relationship between the loss and the magnetic field in the iron region from the perspective of energy conversion. The predictions of magnet loss, sleeve loss, and copper loss using hybrid analytical model agree well with the finite-element method. The experiment on surface-mounted permanent-magnet prototype demonstrates the high accuracy of iron loss calculation using the combination of the improved Jiles-Atherton model and hybrid analytical model.**

Index Terms—**Hybrid analytical model, electromagnetic losses, surface-mounted permanent-magnet motor.**

I. INTRODUCTION

THE permanent-magnet (PM) motors are becoming increasingly popular in the trend of transportation electrification due to their simple structure, high efficiency, and significant power density. They have been used in electric ships, electric airplanes, and electric vehicles [1]-[5]. In these applications, the losses of the PM motors are one of the most significant concerns, as they directly affect the motor efficiency and result in changes in the temperature distribution as well as travel distance of electrified transportation [6]-[7].

The electromagnetic losses of PM motors consist of magnet loss, sleeve loss, copper loss, and iron loss. As the magnet loss,

sleeve loss, and part of copper loss are produced by the eddy current, these losses can be directly calculated based on the eddy current model [8]-[10]. The DC component of copper loss can also be predicted using Ohm's law, or the total copper loss is directly calculated from the magnetic vector potential in the copper region [10]. Since the accurate prediction of the magnetic field in the conductive region is the key to obtaining the magnet loss, sleeve loss, and copper loss, the finite-element method (FEM) shows great advantage over analytical models and magnetic circuit models due to high calculation accuracy [11]. However, it requires extensive calculations due to the small mesh size in PM, sleeve, and copper regions [9]. Nevertheless, this paper will introduce the hybrid analytical model (HAM) to predict the eddy current loss in these regions with excellent accuracy.

For the iron loss model, even if the magnetic field in the iron region can be accurately predicted using FEM, there is a lack of practical method to calculate the iron loss based on the iron field distribution [12]. Steinmetz's equation was often used to estimate the iron loss of PM motors due to the simple form [13]. According to Bertotti's theory, iron loss consists of hysteretic loss, classical eddy-current loss, and anomalous loss, and these terms are all expressed in the form of Steinmetz's equation [14]. Then, the commercial software Ansys Electronics modified the hysteresis loss model in [14] to obtain the instantaneous iron loss [15]. However, the accuracy of these methods in [14]-[15] is significantly affected by the waveform of iron flux density.

The Jiles-Atherton (JA) model is capable of describing magnetic hysteresis using the first-order differential equation [16]. In [17], The PWM-induced iron loss of IPM motor was predicted using the modified JA model. The magnetic field for the JA model was all obtained from FEM, which is also time-consuming. Besides, it is difficult and time-consuming to obtain JA parameters, according to [18]-[19]. It is only possible to extract saturation magnetization M_s from data sheets of electrical steel when the flux density or the magnetization was given under the extremely high magnetic field strength. However, it has not been clear to identify other JA parameters from the measured hysteresis loop [19].

To improve the calculation speed, the magnetic circuit models were applied to analyze the iron loss in single-phase induction motors [20] and axial flux PM motors [21] with less computational burden than FEM. However, it is difficult to calculate the eddy current loss in the conductive region due to the relatively low accuracy of the magnetic field. Although [22] develops an equivalent magnetic circuit model to predict eddy current, there is no FEM or experimental validation.

The conventional analytical model is derived from Poisson's and Laplace's equation for slotless motors. Leandro *et al.* compared several iron loss models for calculating the iron loss of slotless surface-mounted permanent-magnet motors (SPM) based on this analytical model [23]. As for the eddy current loss, the subdomain technique [24]-[28] or the conformal mapping [29] for SPM was used to obtain this loss in the conductive region (e.g., PM region, sleeve region, or copper region). However, these methods all neglect iron saturation [23]-[29].

To improve the accuracy of the analytical and magnetic circuit model for predicting iron loss and eddy current loss in copper, PM, and sleeve, there are additional attempts to combine these models while keeping calculation efficiency compared with FEM [30]-[33]. The magnet loss and iron loss based on the combined analytical model were derived in [34] for external-rotor PM motors and in [35] for spoke-type PM motors, respectively. However, they all lack comprehensive study about the total losses, including iron loss, magnet loss, sleeve loss, and copper loss for the PM motors based on the same analytical model.

In this paper, the HAM that combines conformal mapping technique and magnetic reluctance network is proposed to accurately describe the magnetic field in both the conductive region and iron region. The equivalent current of nonlinearity is introduced from iterative calculation to account for iron saturation. Unlike most analytical models which are only suitable for predicting back-EMF and torque, the proposed model shows excellent accuracy in predicting electromagnetic losses. The losses in the copper, PM, and sleeve are directly obtained from the analytical field distribution in the conductive region. For the iron loss in the stator and rotor, the improved JA model is developed considering the influence of magnetic field level on hysteresis loss. The JA parameters are extracted from the experiment of electrical steel. The FEM and experimental results show the high accuracy of HAM in electromagnetic losses with excellent computational efficiency, making it a competitive candidate for improving the initial design of PM motors. Besides, unlike most analytical models that often focus on one kind of motor losses, HAM could accurately predict all the electromagnetic losses, which is a comprehensive study in this research field.

II. HYBRID ANALYTICAL MODEL

The HAM neglects the end effect of the PM motor and assumes the relative permeability of PM is one. It consists of two parts to predict the magnetic field and electromagnetic losses in the SPM motors, i.e., the analytical model in the linearly permeable region and the magnetic reluctance network in the iron region. The flux source and the equivalent current of nonlinearity are the bridge to connect these two parts based on the boundary condition between two different materials.

As the normal components of flux density are continuous across the boundary, the flux source φ_{ki} flowing into the magnetic reluctance network of iron is calculated using the magnetic vector potential A_{z_lp} from the analytical model in the linearly permeable region.

$$\varphi_{ki} = \varphi_{k\_lp} = \left[A_{z\_lp}(r_{ki}, \alpha_{ki}) - A_{z\_lp}(r_{kj}, \alpha_{kj}) \right] l_{ef} \quad (1)$$

where (r_{ki}, α_{ki}) and (r_{kj}, α_{kj}) are the two ends of the boundary.

They are also displayed using the green dot in Fig. 1, where $k=sy, st, sa, stt, ry$, and i, $j =1,2,3\cdots$. l_{ef} is the effective length of the motor. It can be seen that the flux distribution in the linearly permeable region will affect the saturation level in the iron.
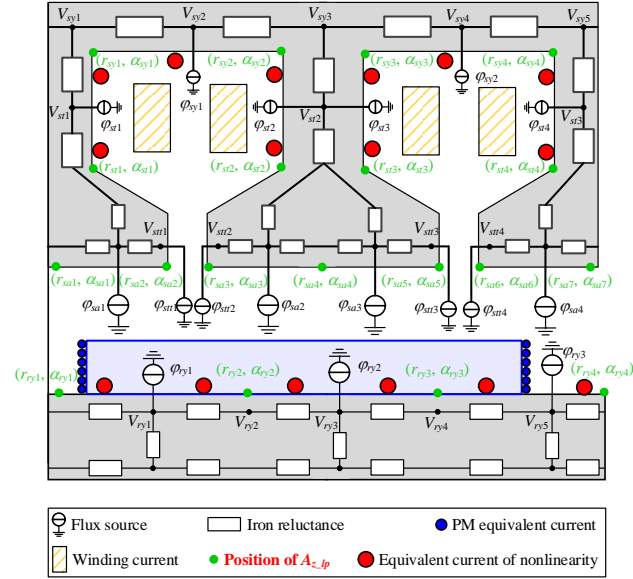

Fig. 1 The general magnetic reluctance network for the HAM.

Meanwhile, the tangential components of magnetic field strength between iron region H_{t_iron} and the linearly permeable region H_{t_lp} are also continuous due to the absence of surface current density.

$$H_{t\_lp} = H_{t\_iron} = \frac{V_{ki} - V_{kj}}{l_k} \quad (2)$$

where V_{ki} and V_{kj} represent the magnetic scalar potential in the magnetic reluctance network of Fig. 1 and l_k is the length of the boundary. To satisfy the premise of the analytical model that the iron permeability should be infinite, the equivalent current sheet of nonlinearity J_{iron} is introduced to replace the tangential magnetic field strength in the iron

$$\begin{cases} H_{t\_iron} = 0 \\ J_{iron} = \dfrac{V_{ki} - V_{kj}}{l_k} \end{cases} \quad (3)$$

It is noted that (3) is only valid for solving the magnetic vector potential in the analytical model and the iron saturation is quantified in the analytical model based on the flux distribution of the iron region.

A. Conformal mapping technique

The conformal mapping function (4) transforms the slotted domain into the slotless domain while preserving the magnetic potential, as shown in Fig. 2 [32].

$$S(r_s, \alpha_s) = h_{cm}(r_\psi, \alpha_\psi) = e^{f_{SC}\left(\frac{b_r}{2\pi} \left[j\log(r_\psi) - \alpha_\psi + \pi \right] + j\frac{a_r}{2} \right)} \quad (4)$$

where (r_s, α_s) and (r_ψ, α_ψ) represent the same position in the slotted and slotless domain, respectively. f_{SC} is the Schwarz-Christoffel mapping that can transform the rectangle into a polygon. a_r and b_r are the width and height of the rectangle, respectively [32]. Hence, as shown in Fig. 2, the magnetic field at the red dot (r_{sp}, α_{sp}) produced by the current at the blue dot

(r_{sc}, α_{sc}) in the slotted domain is equivalently transformed to that at another red dot $(r_{\psi p}, \alpha_{\psi p})$ generated by the current at another blue dot $(r_{\psi c}, \alpha_{\psi c})$ in the slotless domain. The current value keeps the same. The magnetic field in the slotless domain can be analytically expressed as [32]

$$A_{z\psi}(r_{\psi p}, \alpha_{\psi p}, \ r_{\psi c}, \alpha_{\psi c}) = \frac{\mu_0 i_0}{2\pi} \sum_{k=1}^{+\infty} \ln d_0 - \left\{ \cos\left[k\left(\alpha_{\psi p} - \alpha_{\psi c}\right)\right]\right\} \cdot$$
$$\left\{ \frac{r_{\psi r}^{2k}\left[r_{\psi p}^{k} r_{\psi s}^{-k}\left(r_{\psi c}^{2k} r_{\psi r}^{-2k} +1\right) + r_{\psi p}^{-k} r_{\psi s}^{k}\left(r_{\psi s}^{-2k} r_{\psi c}^{2k} +1\right)\right]}{k\left(r_{\psi s}^{2k} - r_{\psi r}^{2k}\right)}\right\} \quad (5)$$
$$= i_0 g_{cm}(r_{\psi p}, \alpha_{\psi p}, r_{\psi c}, \alpha_{\psi c})$$

where d_0 is the distance between the current position and $(r_{\psi c}, \alpha_{\psi c})$ and magnetic field positions $(r_{\psi p}, \alpha_{\psi p})$. i_0 is the value of current. $r_{\psi r}$, and $r_{\psi s}$ are the inner and outer radii of the slotless domain. These symbols are also displayed in Fig. 2. According to the theory of conformal mapping, the slotted airgap field can be obtained as

$$A_{zs}(r_{sp}, \alpha_{sp}, r_{sc}, \alpha_{sc}) = A_{zs}\left(h_{cm}(r_{\psi p}, \alpha_{\psi p}), h_{cm}(r_{\psi c}, \alpha_{\psi c})\right)$$
$$= i_0 g_{cm}(r_{\psi p}, \alpha_{\psi p}, r_{\psi c}, \alpha_{\psi c})$$
$$= i_0 g_{cm}(h_{cm}^{-1}(r_{sp}, \alpha_{sp}), h_{cm}^{-1}(r_{sc}, \alpha_{sc})) \quad (6)$$
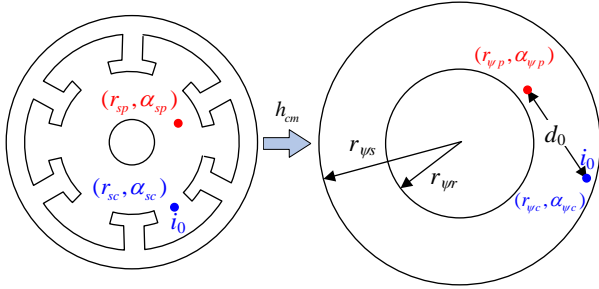$$= i_0 f_{cm}(r_{sp}, \alpha_{sp}, r_{sc}, \alpha_{sc})$$

Fig. 2 The transformation from slotted domain to slotless domain based on conformal mapping.

Accordingly, the radial and tangential flux density at (r_{sp}, α_{sp}) produced by the current at (r_{sc}, α_{sc}) in Fig. 2 is obtained from the derivative of $A_{zs}(r_{sp}, \alpha_{sp}, r_{sc}, \alpha_{sc})$ in (6).

$$B_{rs}\left(r_{sp}, \alpha_{sp}, r_{sc}, \alpha_{sc}\right) = \frac{1}{r_{sp}} \frac{\partial A_z\left(r_{sp}, \alpha_{sp}, r_{sc}, \alpha_{sc}\right)}{\partial \alpha_{sp}}$$
$$B_{\alpha s}\left(r_{sp}, \alpha_{sp}, r_{sc}, \alpha_{sc}\right) = -\frac{\partial A_z\left(r_{sp}, \alpha_{sp}, r_{sc}, \alpha_{sc}\right)}{\partial r_{sp}} \quad (7)$$

It is noted that the dot current i_0 in Fig. 2 can represent PM equivalent current, winding current, and equivalent current of nonlinearity. According to (4)-(6), the value and position of all the equivalent currents are required to obtain the analytical solution for PM motors. The winding current i_{ci} at $(r_{scci}, \alpha_{scci})$ can be directly obtained according to the input current source and winding layout. For the equivalent current of PM i_{PMj}, it is uniformly distributed at $(r_{scPMj}, \alpha_{scPMj})$ along the boundary of PM and it is expressed as

$$i_{PMj}(r_{scPMj}, a_{scPMj}) = \frac{B_r h_m}{\mu_0 N_{PM}} \quad (8)$$

where B_r and h_m are the remanence and length of PM with N_{PM} pairs of equivalent currents [32]. μ_0 is vacuum permeability.

As for the equivalent current of nonlinearity, it is located at $(r_{scnm}, \alpha_{scnm})$ using red dots along the rotor surface and slot region near the stator tooth and yoke to account for rotor and stator saturation in the analytical model, as shown in Fig. 1. The equivalent current of nonlinearity i_{nm} is derived from (3)

$$i_{nm}(r_{scnm}, a_{scnm}) = V_{ki} - V_{kj} \quad (9)$$

The motor rotation is described using the relationship between the current position and the time t.

$$\begin{cases} \alpha_{scPMj} = \omega_r t + \alpha_{scPMj0} \\ \alpha_{scnm} = \omega_r t + \alpha_{scnm0} \end{cases} \quad (10)$$

where α_{scPMj0} and α_{scnm0} are the initial angles of the equivalent current of PM and rotor saturation. w_r is the angular speed of the motor. It is noted that the rotor rotation only changes the values of the flux source flowing into the magnetic reluctance network of iron while keeping the structure of the magnetic reluctance network unchanged. Accordingly, the total magnetic potential A_{z_lp} at the position (r_{sp}, α_{sp}) in the PM, copper, or sleeve region can be obtained according to the superposition principle

$$A_{z\_lp}(r_{sp}, \alpha_{sp}) = \sum_{i=1}^{2Q_s N_c} A_{zs\_winding}(r_{sp}, \alpha_{sp}, r_{scci}, \alpha_{scci})$$
$$+ \sum_{j=1}^{2pN_{PM}} A_{zs\_PM}(r_{sp}, \alpha_{sp}, r_{scPMj}, \alpha_{scPMj0}, t)$$
$$+ \sum_{m=1}^{6p} A_{zs\_nonlinear}(r_{sp}, \alpha_{sp}, r_{scnm}, \alpha_{scnm0}, t) \quad (11)$$
$$+ \sum_{m=6p+1}^{6p+5Q_s} A_{zs\_nonlinear}(r_{sp}, \alpha_{sp}, r_{scnm}, \alpha_{scnm})$$
$$= \sum_k i_k f_{cm}(r_{sp}, \alpha_{sp}, r_{sck}, \alpha_{sck})$$

where A_{zs_PM}, $A_{zs\_winding}$, and $A_{zs\_nonlinear}$ are the magnetic potential produced by PM at the position $(r_{scPMj}, \alpha_{scPMj})$, winding current at the position $(r_{sccj}, \alpha_{sccj})$, and equivalent current of nonlinearity at the position $(r_{scnm}, \alpha_{scnm})$, respectively. $k=ci, PMj, nm$. Q_s and p are the numbers of slots and poles for the motor. N_c is the number of conductors per slot for each phase.

B. Magnetic reluctance network

The magnetic reluctance network can calculate the magnetic field in the PM motors considering the iron nonlinearity. The flux in the iron region, e.g., stator tooth and stator yoke, is usually uniformly distributed in the regular area, making the prediction of the iron field accurate. The magnetic resistance of iron can represent two kinds of shapes, i.e., rectangle and sector, to form the corresponding network for the whole stator and rotor. For the flux flowing through the rectangle, the magnetic resistance is expressed as

$$R_{rec} = \frac{a_i}{\mu_{iron} l_{ef} b_i} \quad (12)$$

and for the flux flowing through the sector, the magnetic resistance is expressed as

$$R_{sec\_r} = \frac{\ln(r_{sec2}/r_{sec1})}{\mu_{iron} l_{ef} \theta_{sec}} \quad (13)$$

in the radial direction and

$$R_{\text{sec}\_t} = \frac{\theta_{\text{sec}}}{\mu_{iron} l_{ef} \ln(r_{\text{sec}2}/r_{\text{sec}1})} \quad (14)$$

in the tangential direction, where a_i and b_i are the width and height of the rectangle. u_{iron} is the iron permeability. θ_{rec}, r_{sec2}, and r_{sec2} are the sector's angle, outer and inner radii.

Then, the stator yoke, stator tooth-tip, and rotor yoke in the SPM can be divided into several sectors, while every stator tooth can be represented using two rectangles. Their corresponding reluctance network is established in Fig. 1, and the values of the magnetic resistance are calculated using (12)-(14). It is noted that the iron permeability u_{iron} can only be determined iteratively due to the nonlinear magnetic property of iron. Suppose the magnetic resistance of air, sleeve, PM, and copper is used in the magnetic reluctance network of Fig. 1. In that case, it becomes a traditional circuit-based model for calculating the magnetic field of the PM motor. However, as the air flux is irregular, it is difficult to obtain a general network in the PM, airgap, and slot-opening region without increasing magnetic resistance for the circuit-based model.

C. Hybrid analytical model

Compared with the circuit-based model, the hybrid analytical model can accurately calculate the flux of airgap, PM, and copper while reducing the size of the magnetic reluctance network significantly. The analytical approach is used to solve the problem of calculating the irregular airgap flux and unequal potential along the PM surface based on the circuit-based model. The general equation of magnetic potential matrix $\mathbf{V}$ for HAM is:

$$g(\mathbf{V}) = \mathbf{A_N}\mathbf{\Lambda_N}\mathbf{A_N^T}\mathbf{V} - \mathbf{\Phi_N} = \mathbf{0} \quad (15)$$

where $\mathbf{A_N}$ represents the constant relationship between the branch flux and node voltage. $\mathbf{\Lambda_N}$ is the nonlinear matrix of the magnetic resistance for the iron. $\mathbf{\Phi_N}$ is the matrix of flux source φ_{ki}, e.g., φ_{sy1}, φ_{st1}, φ_{sa1}, φ_{stt1}, φ_{sry1}, φ_{sy2} in Fig. 1. Then, (15) is manipulated to solve $\mathbf{V}$ iteratively using the recursive Newton's method

$$\mathbf{V_{i+1}} = \mathbf{V_i} - \alpha_0 \frac{g(\mathbf{V_i})}{\mathbf{A_N}\mathbf{\Lambda_{N(i)}}\mathbf{A_N^T}} \quad (16)$$

where α_0 is the relaxation factor and $\mathbf{\Lambda_N}$ is updated using the BH curve of the iron at every iteration. When the initial value $\mathbf{V_1}$ is assigned, it will reach to the convergent value of $\mathbf{V}$ in (15) and determine the final iron permeability based on BH curves. The stopping criterion for the iteration process is $g(\mathbf{V_{i+1}}) \le 0.0001 \times \max(\mathbf{\Phi_N})$, and the magnetic field of the whole PM motor considering iron nonlinearity will be returned.

III. ELECTROMAGNETIC LOSSES OF PM MOTORS

A. Iron loss

The iron loss of SPM is calculated using the improved JA model. The mathematical equation for describing static hysteresis loops of electrical steel is expressed as [16]

$$\begin{cases} M = M_{irr} + M_{rev} \\ M_{rev} = c(M_{an} - M_{irr}) \\ M_{an} = M_s (\coth(\frac{H_e}{a}) - (\frac{a}{H_e})) \\ H_e = H_{hys} + \alpha M \\ \mu_0 \int M_{an} dH_e = \mu_0 \int M dH_e + \mu_0 k\delta(1-c)\int (\frac{dM_{irr}}{dH_e})dH_e \end{cases} \quad (17)$$

where M_{rev} and M_{irr} represent the reversible and irreversible components of the total magnetization M. H_e is the effective field. H_{hys} is the static hysteresis field. The five JA parameters are defined as follows: M_s represents saturation magnetization; a represents the domain wall density; c quantifies magnetization reversibility; α represents interdomain coupling; k represents average energy for breaking pining site. $\delta=\pm1$ to guarantee the lost energy in the dissipation. The static hysteresis loss is considered to be only related to the flux density amplitude B_m and electrical frequency f

$$P_{hys} = f \cdot A_{hys}(B_m) \quad (18)$$

where $A_{hys}(B_m)$ represents the area of the static hysteresis loop.

To consider the influence of frequency in the BH loop, the effective field H_e in (17) is modified according to Bertotti's theory [14]

$$H_{total} = H_{hys}(B_m) + H_{eddy} + H_a \quad (19)$$

where H_{total} represents the total field. H_{eddy} and H_a are the classical eddy-current field and the anomalous field. The time average classical eddy-current loss and the corresponding eddy-current field are given as [16]

$$P_{eddy} = \frac{d^2}{2\rho\beta} \frac{1}{T_p} \int_0^{T_p} \left(\frac{dB}{dt}\right)^2 dt \quad (20)$$

$$H_{eddy} = \frac{d^2}{2\rho\beta} \frac{dB}{dt} \quad (21)$$

where ρ and d are the resistivity and thickness of the magnetic material. β is a geometrical parameter. T_p is the period of the flux density.

The anomalous loss results from the bowing of active domain or discontinuous Barkhausen jump walls in electrical steels. It will induce magnetic flux and lead to Ohmic loss. The anomalous field is given as [14]

$$H_a = \frac{GS}{\rho \cdot n(t)} \left(\frac{dB}{dt}\right) \quad (22)$$

where G is the dimensionless coefficient, S is the cross-section of electrical steels and $n(t)$ is the number of active correlation regions randomly distributed in the cross-section. Besides, H_a and $n(t)$ have another relation to representing the magnetization processes.

$$n(\text{t}) = n_0 + \frac{H_a(t)}{H_0} \quad (23)$$

where n_0 and H_0 represent the statistical distribution of the internal domain wall field. Thus, the instantaneous anomalous field and the time average anomalous loss can be given as [14]

$$H_a = \frac{1}{2}\left(\sqrt{n_0^2 H_0^2 + \frac{4GSH_0}{\rho}\left|\frac{dB}{dt}\right|} - n_0 H_0 \right)$$
$$\approx \sqrt{\frac{GSH_0}{\rho}\left|\frac{dB}{dt}\right|} \tag{24}$$

$$P_a = \frac{1}{T_p}\int_0^{T_p} \sqrt{\frac{GSH_0}{\rho}} \cdot \left|\frac{dB}{dt}\right|^{\frac{3}{2}} dt \tag{25}$$

Thus, the total iron loss is calculated as
$$P_{iron} = P_{hys} + P_{eddy} + P_a \tag{26}$$

Even though the improved JA model is established using (17)-(26), extracting JA parameters is one of the major challenges to accurately predict iron loss. Fig. 3 illustrates the calculation process based on the improved JA model. For the parameters of classical eddy-current loss in (20), they are provided by the manufacturer. For the parameters of anomalous loss, the literature shows that the anomalous loss parameter H_0 can be either directly obtained from the measured BH loop using a differential evolution algorithm [38] or calculated using iron loss at a different frequency [39]. However, these approaches are easily affected by the accidental error of dynamic BH loop and iron loss measurement. Therefore, this paper proposed the linear regression to identify H_0 in (25). To achieve the linear fitting of H_a and $n(t)$ based on (23), the time average of active correlation regions $\tilde{n}$ is obtained from (22) when the iron flux density is sinusoidal

$$\tilde{n} = \frac{2\pi^2 GSB_m^2 f^2}{\rho P_a} \tag{27}$$

Meanwhile, the time-averaged anomalous field $\tilde{H}_{excess}$ is obtained from (24) for the sinusoidal flux density

$$\tilde{H}_{excess} = \frac{P_a}{4B_m f} \tag{28}$$

Thus, H_0 is obtained from the slope of the regression line between $\tilde{n}$ and $\tilde{H}_a$ using (23). To obtain the anomalous loss P_a from the total iron loss, the static hysteresis losses are represented using the measured iron loss at 3 Hz and the classical eddy-current losses are predicted using (20).
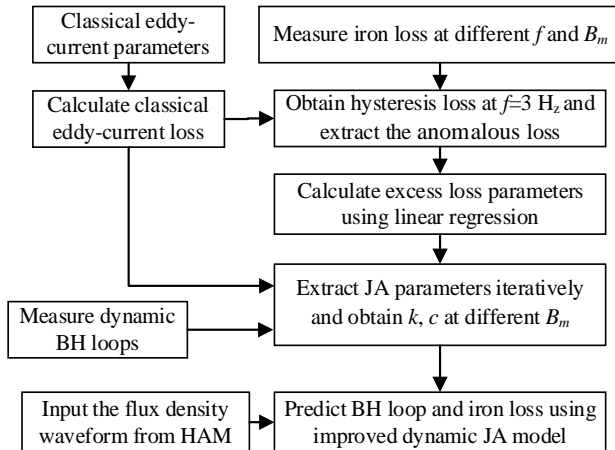

Fig. 3 The flowchart of extracting JA parameters and predicting iron loss.

After extracting the parameters of anomalous loss and classical eddy-current, the five JA parameters (a, α, c, k, M_s) are obtained from the measured BH loop using differential evolution algorithm based on (17) and (19) iteratively. It is noted that a, α, and M_s keep unchanged at different amplitudes of flux density B_m while the variation of k and c to B_m is determined for the improved JA model with iteration. The objective function of the differential evolution algorithm is to minimize the differences between the measured and predicted BH loops.

$$obj = \frac{\sum_{i=1}^{n} \left| H_{pre}(i) - H_{mea}(i) \right|}{n \cdot \max(H_{mea})} \tag{29}$$

where H_{pre} and H_{mea} are the predicted and measured magnetic fields in iron, respectively. It can also represent the error of the predicted dynamic BH loop.

B. Eddy current loss in conductive region

When neglecting the end effect, the eddy-current and the instantaneous eddy-current loss in the conductive region are expressed as

$$J_{eddy}(r_{sp}, \alpha_{sp}, t) = -\sigma \frac{\partial A_{z\_lp}(r_{sp}, \alpha_{sp})}{\partial t} + C_{lp}(t) \tag{30}$$

$$p_e = \frac{l_{ef}}{\sigma}\int_{\alpha_{sp1}}^{\alpha_{sp2}} \int_{r_{sp1}}^{r_{sp2}} J_{eddy}^2(r_{sp}, \alpha_{sp}, t) r_{sp} dr_{sp} d\alpha_{sp} \tag{31}$$

where σ is the conductivity of the material. r_{sp2} and r_{sp1} are the external and internal radii of the conductive region. α_{sp2} and α_{sp1} are the upper and lower edge of the conductive region. Segmenting the PM in the radial or tangential direction changes the value of α_{sp2} and α_{sp1} or r_{sp1} and r_{sp1}, respectively, and thus changes the magnet loss. For the sleeve loss, $\alpha_{sp1}=0$ and $\alpha_{sp2}=2\pi$ while $r_{sp2}=R_{rs}$ and $r_{sp1}=R_m$, where R_{rs} is the external radius of the sleeve and R_m is the external radius of the PM. Since the total eddy-current in the single conductor should be equal to zero for the PM and sleeve, $C_{lp}(t)$ is calculated using

$$C_{lp}(t) = \frac{2\sigma \sum_{l=1}^{N_t} \int_{\alpha_{sp1}}^{\alpha_{sp2}} \int_{r_{sp1}}^{r_{sp2}} \frac{\partial A_{z\_lp}}{\partial t} r_{sp} dr_{sp} d\alpha_{sp}}{(\alpha_{sp2} - \alpha_{sp1})(r_{sp2}^2 - r_{sp1}^2)} \tag{32}$$

The AC and DC components of the copper loss are also calculated using (31), where $C_{lp}(t)$ is expressed as

$$C_{lp}(t) = J_{copper}(t) + \frac{2\sigma \sum_{l=1}^{N_t} \int_{\alpha_{sp1}}^{\alpha_{sp2}} \int_{r_{sp1}}^{r_{sp2}} \frac{\partial A_{z\_lp}}{\partial t} r_{sp} dr_{sp} d\alpha_{sp}}{(\alpha_{sp2} - \alpha_{sp1})(r_{sp2}^2 - r_{sp1}^2)} \tag{33}$$

where $J_{copper}(t)$ represents the current density in each coil. To simplify the calculation, it is assumed that the cross-section of the coil is fan-shaped and keeps the same area as the actual copper wire. Therefore, α_{sp2}, α_{sp1}, r_{sp1}, and r_{sp1} represent the position for each coil for copper loss calculation.

C. Solving process

Fig. 4 shows the process of calculating electromagnetic losses using HAM, where the magnetic field of the motor should be obtained first. Then the iron loss model and eddy current loss model are employed for predicting the losses in the

conductive region and iron region, respectively. The flux density waveforms from HAM and the electromagnetic loss coefficients are the main inputs to obtain the values of iron loss and eddy current loss in copper, PM, and sleeve.
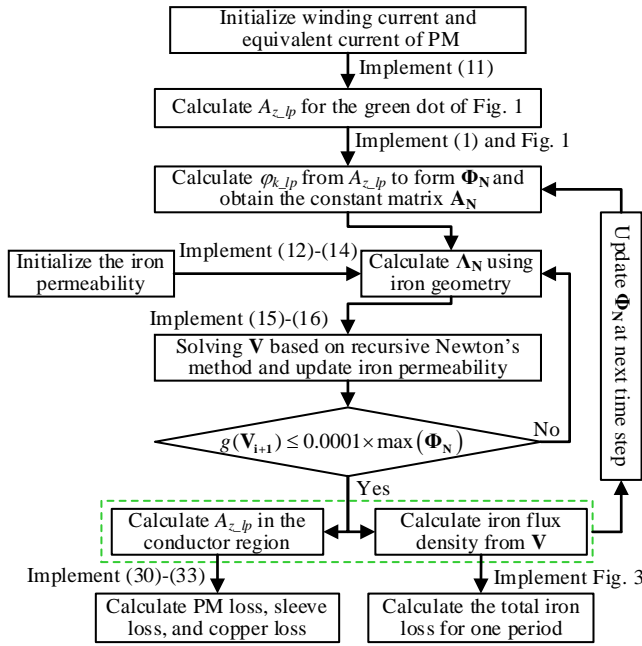

Fig. 4 The solving process of calculating electromagnetic losses using HAM.

IV. FE AND EXPERIMENTAL VALIDATION

A. FEM validation

A 4-pole 36-slot SPM is designed and analyzed to illustrate the calculation accuracy and efficiency of the proposed model, Fig. 5. The stainless-steel sleeve is used to guarantee the mechanical strength of rotor. The coil is uniformly distributed in each slot. The main parameters are given in Table I.
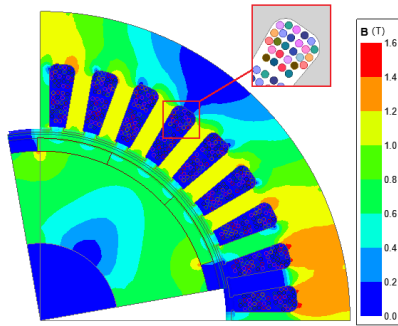

Fig. 5 The flux density distribution of SPM at 30A.

TABLE I
THE MAIN PARAMETERS OF THE PM MOTOR.

Parameter	Value	Parameter	Value
Pole number	4	Slot number	36
Stator outer diameter	120 mm	Rotor outer diameter	72.4 mm
Stator inner diameter	74 mm	Magnet thickness	2.5 mm
Stator yoke height	10.1 mm	Shaft diameter	30 mm
Slot opening	2.5 mm	Tooth body width	3.4 mm
Thickness of sleeve	0.8 mm	Active length	70 mm
Iron material	20JNEH1200	Magnet material	N35UH

The comparisons of the on-load magnetic field in the airgap between the FEM and HAM are given in Fig. 6. The analytical prediction agrees well with FEM results, which is fundamental

for the eddy current loss in the conductive region. Table II shows that HAM can significantly reduce the calculation time compared with FEM. However, as the FEM is employed based on the commercial software ANSYS Electromagnetics while HAM is operated in MATLAB, there is a significant gap between FEM and HAM in the efficient programming and optimized algorithm. Hence, even though the node number of FEM is 70 times larger than that of HAM in Table II, HAM consumes about 1/8 of the solving time using FEM. Then, the magnet loss, sleeve loss, and copper loss are obtained based on HAM using (30)-(33) at different working conditions, Fig. 7-Fig. 9. They all show high accuracy compared with FEM calculation.
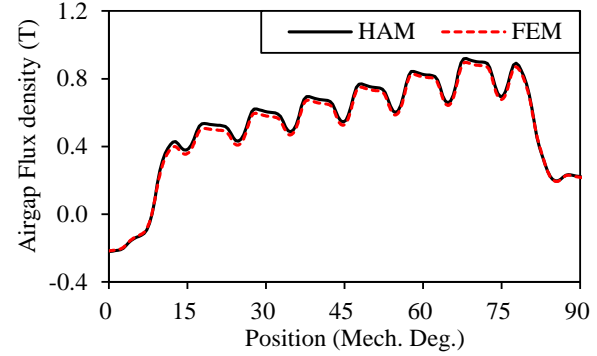
(a) radial direction
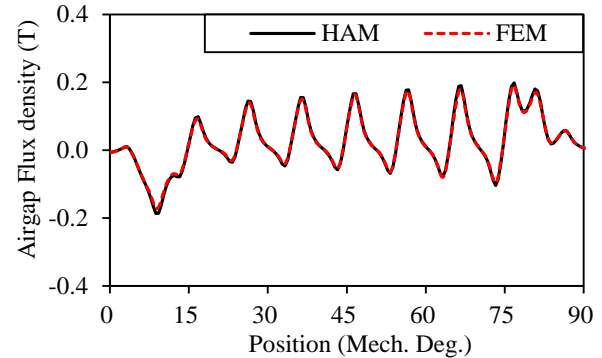
(b) tangential direction

Fig. 6 The comparison of on-load magnetic field using FEM and HAM

TABLE II
THE SIMULATION PARAMETERS OF FEM AND HAM

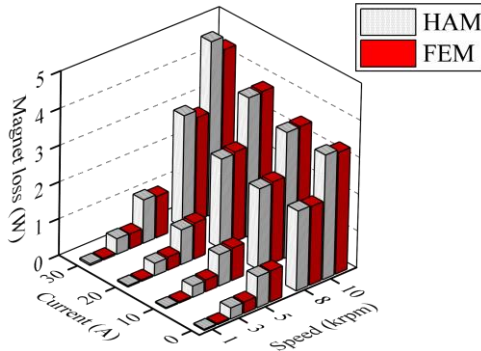| Model	Node in the iron	Node in the copper/PM/sleeve	Current	Solving time
FEM	13659	192460	0 A	28 min
			30 A	21min
HAM	186	2232	0 A	2.5 min
			30 A	2.6 min

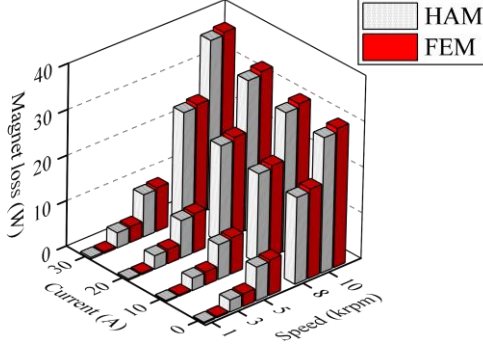Fig. 7 The magnet loss of SPM at different working conditions.

Fig. 8 The sleeve loss of SPM at different working conditions.
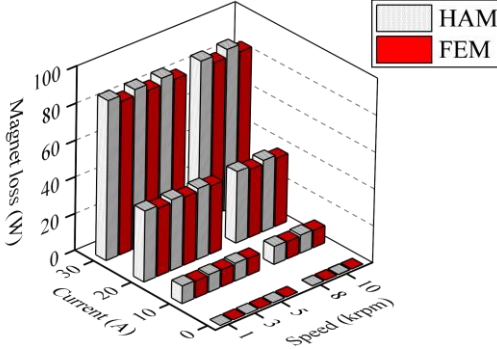

Fig. 9 The copper loss of SPM at different working conditions.

B. Experimental validation of the electrical steel

To accurately model and predict the iron loss in the SPM, the loss data of electrical steel (20JNEH1200) should be obtained first from an Epstein frame based on TD8510 Testing System from Tunkia Ltd, China, Fig. 10. The frequency dependency of iron loss in the JA model is represented using the eddy-current loss coefficient C_e and the anomalous loss coefficient C_a. According to the dimension and resistivity of the electrical steel, C_e=6.1×10^{-3} m/Ω, which is calculated using (20). In addition, the anomalous loss coefficient C_a is extracted from the relationship between the number of active correction regions n and average anomalous field H_a under the excitation of sinusoidal flux density, Fig. 11. The BH loop and hysteresis loss of 20JNEH1200 at 3 Hz is measured and displayed in Fig. 12, from which the JA parameters can be obtained to predict the static BH loops at different amplitudes of flux density. Table III shows that the JA parameters k, c, and C_a are affected by the amplitude of flux density in the proposed JA model while other JA parameters M_s, a, and α keep unchanged [40]. For the electrical steel in this SPM, M_s=1.3×10^6 A/m, a= 70.6 A/m, α=1.18×10^{-4}.

Fig. 10 TD8510 testing system for the magnetic property of electrical steel.
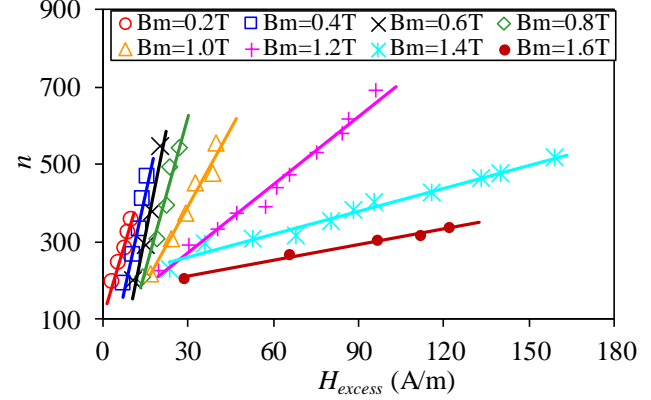

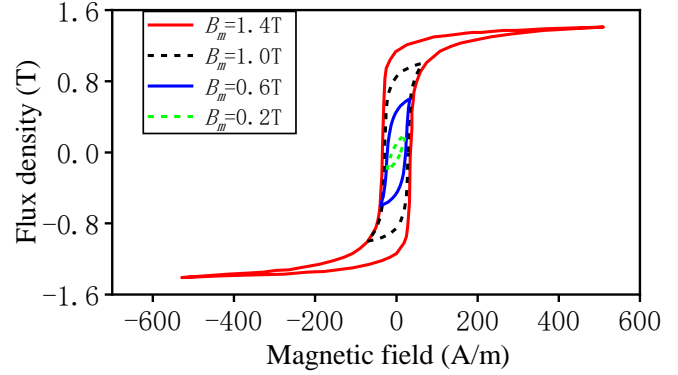Fig. 11 The variation of n to Ha with sinusoidal flux density.

Fig. 12 The variation of BH loops for 20JNEH1200 to flux density at 3 Hz in the Epstein frame.

TABLE III
THE JA PARAMETERS FOR THE ELECTRICAL STEEL 20JNEH1200

B_m (T)	c	k (A/m)	C_a (A/Ω)$^{1/2}$
1.6	0.95	46	1.04
1.4	0.89	18	0.86
1.2	0.54	28	0.50
1.0	0.39	29	0.33
0.8	0.33	34	0.24
0.6	0.31	39	0.20
0.4	0.41	34	0.21
0.2	0.46	43	0.25

C. Experimental validation on a PM motor

As the improved JA model is effective for the electrical steel lamination, the nonlinear analytical model, which can extract the magnetic field, is combined with the improved JA model to predict the iron loss distribution in the stator and rotor of the SPM. Fig. 13(a) shows the 4-pole 36-slot SPM prototype was tested using the dynamometer DW20KB from Weiheng Technology, whose torque error is less than 0.3% and speed error is less than 1 rpm. In the test rig, the input and output power of the motor was recorded by the power analyzer

TOKOGAWA WT1800 to obtain the total loss. The motor current was measured using the oscilloscope Tektronix MDO34 and the copper loss was calculated, as the eddy current effect was neglected in the copper region due to the low electrical frequency in the experiment. Besides, the mechanical loss of the prototype was measured when the stator of the prototype was removed. Another dynamometer in Fig. 13(b) was used as the prime motor to rotate the prototype. The mechanical loss of the prototype was equal to the output power of the dynamometer from the measurement of torque and speed.

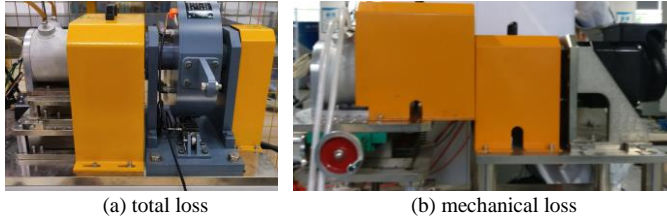(a) total loss   (b) mechanical loss

Fig. 13 The test rig for electromagnetic loss evaluation in a SPM.

    The average torque is measured and compared with HAM and FEM to show the high accuracy of the proposed model, Fig. 14. The flux density in the stator region is obtained from the magnetic reluctance network in HAM, which agrees well with FEM in Fig. 15(a). Then, the dynamic BH loop can be calculated using the iron field distribution and improved JA model, as shown in Fig. 15(b).
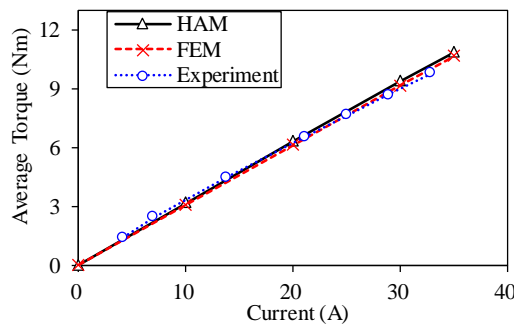

Fig. 14 The comparison of average torque in the SPM using HAM, FEM, and experiments.

    The commercial inverter was used to drive the SPM motor, where the harmonic current occurred due to the PWM effect. As the harmonic components of the winding current are small under load condition from measurement, they are neglected to reduce computational burden. Fig. 16 compares the total electromagnetic losses of the SPM using HAM, FEM, and experiments. As it is difficult to segregate the magnet loss, sleeve loss, and iron loss, this paper compares the total loss from HAM, FEM, and experiment to validate the effectiveness of iron loss prediction. Given that the FEM calculation of magnet loss and sleeve loss can accurately represent the actual loss value [24], [41], the differences between the measured and predicted loss in Fig. 16 are mainly from inaccuracies in the iron loss calculation. The results illustrate that HAM agrees with FEM calculation for the magnet loss and sleeve loss, but outperforms the FEM-based Steinmetz's equation in iron loss prediction. Such improvements mainly come from the excellent extraction of JA parameters for the improved JA model.
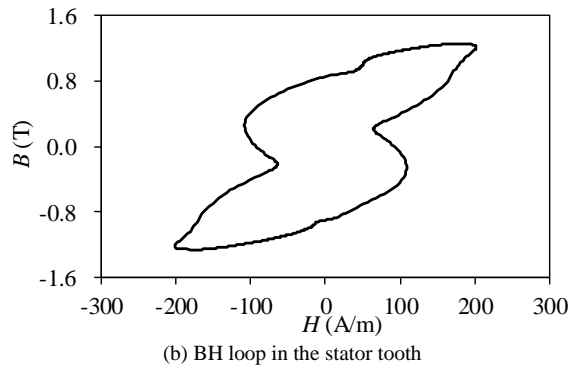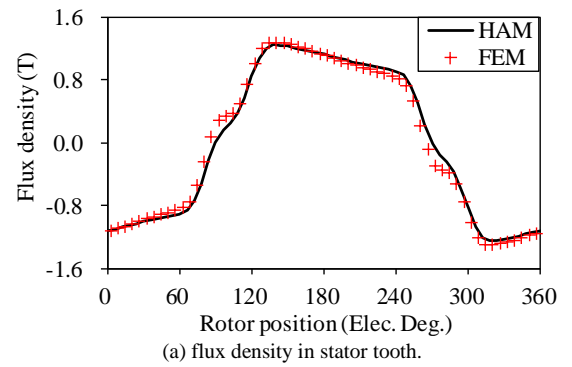

(a) flux density in stator tooth.

(b) BH loop in the stator tooth

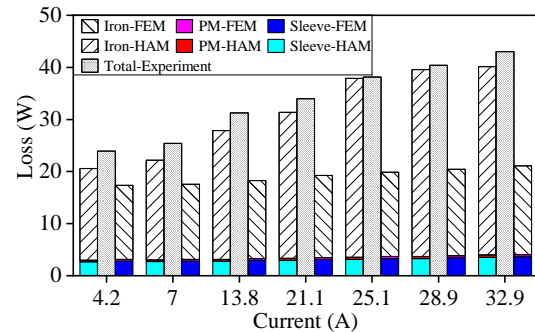Fig. 15 The magnetic property of stator iron in a SPM at 30A.

Fig. 16 The comparison of electromagnetic loss in the SPM.

V. CONCLUSION

    This paper developed a HAM to predict the magnet loss, sleeve loss, copper loss, and iron loss in a SPM considering iron nonlinearity. An analytical model and a magnetic reluctance network represent the magnetic field in the conductive region and iron region, respectively. The eddy current in the conductive region is derived from Faraday's law, while the iron loss is predicted using the improved JA model. The JA parameters are extracted from electrical steel sheet experiments and they are used to estimate the iron loss in the SPM. Both FEM and experiments in the 4-pole 36-slot SPM show the high accuracy of HAM in estimating electromagnetic losses with excellent computational efficiency.

REFERENCES

[1] J. -D. Mira, F. Mendoza, E. Betancur, T. Manrique, and R. Mejía-Gutiérrez, "A propulsion system design methodology based on overall efficiency optimization for electrically powered vessels," *IEEE Trans. Transp. Electrific.,* vol. 8, no. 1, pp. 239-250, 2022.

[2] M. Qiao, C. Jiang, Y. Zhu, and G. Li, "Research on design method and electromagnetic vibration of six-phase fractional-slot concentrated-winding PM motor suitable for ship propulsion," *IEEE Access*, vol. 4, pp. 8535-8543, 2016.

[3] W. Cao, B. C. Mecrow, G. J. Atkinson, J. W. Bennett, and D. J. Atkinson, "Overview of electric motor technologies used for more electric aircraft (MEA)," *IEEE Trans. Ind. Electron.,* vol. 59, no. 9, pp. 3523-3531, 2012.

[4] C. Zhou, X. Huang, Z. Li, and W. Cao, "Design consideration of fractional slot concentrated winding interior permanent magnet synchronous motor for EV and HEV applications," *IEEE Access*, vol. 9, pp. 64116–64126, 2021.

[5] W. Geng, Z. Zhang, and Q. Li, "Analysis and experimental verification of a conventional inverter with output LC filter to drive ironless stator axial-flux PM motor," *IEEE Trans. Transp. Electrific.,* vol. 7, no. 4, pp. 2600-2610, 2021.

[6] W. Li, Z. Cao, and X. Zhang, "Thermal analysis of the solid rotor permanent magnet synchronous motors with air-cooled hybrid ventilation systems," *IEEE Trans. Ind. Electron.,* vol. 69, no. 2, pp. 1146-1156, 2022.

[7] G. Du, W. Xu, J. Zhu, and N. Huang, "Power loss and thermal analysis for high-power high-speed permanent magnet machines," *IEEE Trans. Ind. Electron.,* vol. 67, no. 4, pp. 2722-2733, 2020.

[8] W. Tong, Y. Wang, R. Sun, S. Wu, and J. Jia, "Simulation and experimental study on no-load loss distributions of an IPM motor under the conditions of both sinusoidal supply and converter supply," *IEEE Trans. Magn.*, vol. 54, no. 11, pp. 1–6, Nov. 2018.

[9] T. Han, Y. Wang, and J.X. Shen, "Analysis and experiment method of influence of retaining sleeve structures and materials on rotor eddy current loss in high-speed PM motors," *IEEE Trans. Ind. Appl.,* vol. 56, no. 5, pp. 4889-4895, 2020.

[10] K. Yamazaki, T. Furuhashi, and S. Hara, "Separation of Winding Losses of Permanent Magnet Motors by Considering Eddy Currents and Parallel Circuit Connections', *IEEE Transactions on Magnetics*, vol. 57, no. 6, pp. 1–4, Jun. 2021.

[11] N. Taran, D. M. Ionel, V. Rallabandi, G. Heins, and D. Patterson, "An overview of methods and a new three-dimensional FEA and analytical hybrid technique for calculating AC winding losses in PM machines," *IEEE Trans. Ind. Appl.,* vol. 57, no. 1, pp. 352–362, 2021.

[12] Q. Zhu, Q. Wu, W. Li, M.T. Pham, and L. Zhu, "A general and accurate iron loss calculation method considering harmonics based on loss surface hysteresis model and finite-element method," *IEEE Trans. Ind. Appl.,* vol. 57, no. 1, pp. 374–381, Jan. 2021.

[13] G. Liu, M. Liu, Y. Zhang, H. Wang, and C. Gerada, "High-speed permanent magnet synchronous motor iron loss calculation method considering multiphysics factors," *IEEE Trans. Ind. Electron.,* vol. 67, no. 7, pp. 5360-5368, 2020.

[14] G. Bertotti, "General properties of power losses in soft ferromagnetic materials," *IEEE Trans. Magn.*, vol. 24, no. 1, pp. 621-630, Jan. 1988.

[15] D. Lin, P. Zhou, W. N. Fu, Z. Badics, and Z. J. Cendes, "A dynamic core loss model for soft ferromagnetic and power ferrite materials in transient finite element analysis," *IEEE Trans. Magn.*, vol. 40, no. 2, pp. 1318-1321, Mar. 2004.

[16] D. C. Jiles and D. L. Atherton, "Theory of ferromagnetic hysteresis," *J. Magn. Magn. Mater.*, vol. 61, pp. 48-60, 1986.

[17] L. Chang, T. M. Jahns, and R. Blissenbach, "Estimation of PWM-induced iron loss in IPM machines incorporating the impact of flux ripple waveshape and nonlinear magnetic characteristics," *IEEE Trans. Ind. Appl.,* vol. 56, no. 2, pp. 1332-1345, 2020.

[18] Z. Chen, Y. Yu, and Y. Wang, "Parameter identification of Jiles-Atherton model based on Levy Whale optimization algorithm," *IEEE Access,* vol. 10, pp. 66711-66721, 2022.

[19] D. C. Jiles, J. B. Thoelke and M. K. Devine, "Numerical determination of hysteresis parameters for the modeling of magnetic properties using the theory of ferromagnetic hysteresis," *IEEE Trans. Magn.*, vol. 28, no. 1, pp. 27-35, Jan. 1992.

[20] H. Saneie and Z. Nasiri-Gheidari, "Performance analysis of outer-rotor single-phase induction motor based on magnetic equivalent circuit," *IEEE Trans. Ind. Electron.*, vol. 68, no. 2, pp. 1046-1054, 2021.

[21] R. Z. Haddad, "Iron loss analysis in axial flux permanent magnet synchronous motors with soft magnetic composite core material," *IEEE Trans. Energy Convers.,* vol. 37, no. 1, pp. 295-303, 2022.

[22] J. Wang and J. Zhu, "A simple method for performance prediction of permanent magnet eddy current couplings using a new magnetic equivalent circuit model," *IEEE Trans. Ind. Electron.*, vol. 65, no. 3, pp. 2487-2495, 2018.

[23] M. Leandro, N. Elloumi, A. Tessarolo, and J. K. Nøland, "Analytical iron loss evaluation in the stator yoke of slotless surface-mounted PM machines," *IEEE Trans. Ind. Appl.,* vol. 58, no. 4, pp. 4602-4613, 2022.

[24] W. Tong, L. Sun, S. Wu, M. Hou, and R. Tang, "Analytical model and experimental verification of permanent magnet eddy current loss in permanent magnet machines with nonconcentric magnetic poles," *IEEE Trans. Ind. Electron.,* vol. 69, no. 9, pp. 8815–8824, 2022.

[25] O. de la Barriere, S. Hlioui, H. Ben Ahmed, and M. Gabsi, 'An analytical model for the computation of no-load eddy-current losses in the rotor of a permanent magnet synchronous machine', *IEEE Trans. Magn.,* vol. 52, no. 6, pp. 1–13, Jun. 2016.

[26] Z. Zhang, Z. Deng, Q. Sun, C. Peng, Y. Gu, and G. Pang, "Analytical modeling and experimental validation of rotor harmonic eddy-current loss in high-speed surface-mounted permanent magnet motors," *IEEE Trans. Magn.*, vol. 55, no. 2, pp. 1–11, 2019.

[27] H. Qiu, Z. Zhu, B. Xiong, and C. Yang, "Influence of eddy current loss on electromagnetic field and temperature field of high-speed permanent magnet generator with the toroidal windings," *IEEE Access*, vol. 10, pp. 98259–98267, 2022.

[28] L. J. Wu and Z. Q. Zhu, "Simplified analytical model and investigation of open-circuit ac winding loss of permanent-magnet machines," *IEEE Trans. Ind. Electron.,* vol. 61, no. 9, pp. 4990–4999, 2014.

[29] N. Chiodetto, N. Bianchi and L. Alberti, "Improved analytical estimation of rotor losses in high-speed surface-mounted PM synchronous machines," *IEEE Trans. Ind. Appl.,* vol. 53, no. 4, pp. 3548-3556, 2017.

[30] L. Wu, H. Yin, D. Wang, and Y. Fang, "On-load field prediction in SPM machines by a subdomain and magnetic circuit hybrid model," *IEEE Trans. Ind. Electron.,* vol. 67, no. 9, pp. 7190–7201, Sep. 2020.

[31] Z. Li, X. Huang, L. Wu, H. Zhang, T. Shi, Y. Yan, B. Shi, and G. Yang, "An improved hybrid field model for calculating on-load performance of interior permanent-magnet motors," *IEEE Trans. Ind. Electron.,* vol. 68, no. 10, pp. 9207–9217, 2021.

[32] A. Hanic, D. Zarko, D. Kuhinek, and Z. Hanic, "On-load analysis of saturated surface permanent magnet machines using conformal mapping and magnetic equivalent circuits," *IEEE Trans. Energy Convers.,* vol. 33, no. 3, pp. 915–924, 2018.

[33] J. Ren, X. Wang, and W. Zhao, "Magnetic field prediction of the saturated surface-mounted permanent magnet synchronous machine with rotor eccentricity," *IEEE Trans. Ind. Electron.,* vol. 69, no. 8, pp. 7756-7766, 2022.

[34] Z. Li, X. Huang, X. Xu, Z. Chen, Z. Jiang, L. Wu, T. Shi, and J. Zhang, "Nonlinear analytical model for predicting magnet loss in surface-mounted permanent-magnet motors," *IEEE Trans. Magn.*, pp. 1–5, 2022.

[35] P. Liang, F. Chai, L. Chen and Y. Wang, "Analytical prediction of no-load stator iron losses in spoke-type permanent-magnet synchronous machines," *IEEE Trans. Energy Convers.,* vol. 33, no. 1, pp. 252-259, 2018.

[36] J. Chen, S. Wang, H. Shang, H. Hu, and T. Peng, "Finite Element Analysis of Axial Flux Permanent Magnetic Hysteresis Dampers Based On Vector Jiles-Atherton Model," *IEEE Trans. Energy Convers.,* 2022, in press.

[37] R. Galluzzi, N. Amati, and A. Tonoli, "Modeling, design, and validation of magnetic hysteresis motors," *IEEE Trans. Ind. Electron.,* vol. 67, no. 2, pp. 1171-1179, 2020.

[38] M. Hamimid, S. M. Mimoune, and M. Feliachi, "Hybrid magnetic field formulation based on the losses separation method for modified dynamic inverse Jiles–Atherton model," *Phys.* B., vol. 406, no. 14, pp. 2755–2757, 2011.

[39] R Du and P Robertson, "Dynamic Jiles-Atherton model for determining the magnetic power loss at high frequency in permanent magnet machines," *IEEE Trans. Magn.*, vol. 51, no. 6, pp. 1-10, June 2015.

[40] Z. Li, X. Huang, L. Wu, J. Chen, Y. Zhong, J. Ma, and Y. Fang, "A modified Jiles-Atherton model for estimating the iron loss of electrical steel considering DC bias," in 2018 Thirteenth International Conference on Ecological Vehicles and Renewable Energies (*EVER*2018), Monaco, 2018, pp. 1-7.

[41] D. Golovanov, A. Galassini, T. Transi, and C. Gerada, "Analytical methodology for eddy current loss simulation in armature windings of synchronous electrical machines with permanent magnets," *IEEE Trans. Ind. Electron.,* vol. 69, no. 10, pp. 9761–9770, 2022.